PERGAMON International Journal of Multiphase Flow 26 (2000) 1583–1607

International Journal of Multiphase Flow

www.elsevier.com/locate/ijmulflow

Experiments on particle dispersion in a plane wake

Y. Yang, C.T. Crowe*, J.N. Chung, T.R. Troutt

School of Mechanics and Materials Engineering, Washington State Univerity, Pullman, WA 99164-2920, USA

Received 23 April 1998; received in revised form 10 October 1999

Abstract

Detailed experimental results are presented concerning the effects of vortex structures on the solid particle dispersion process in a plane wake. Previous numerical results have indicated that vortex structures in plane wakes can disperse intermediate Stokes number particles into highly organized patterns. The cross stream spatial dispersion values associated with these particles were computed to be several times greater than that associated with fluid elements. The major objective of this study was to obtain direct experimental results concerning the time dependent particle dispersion process in a plane wake. The experimental approach used in this work primarily involves laser sheet pulsed imaging of glass bead particles in a wake downstream of a blunt trailing edge. Two sizes of glass beads with nominal diameters of 10 and 30 μm were used as particles in an air flow. The associated Stokes numbers of the particles were 0.15 and 1.4. Digital image analysis techniques were employed to identify and determine particle locations and velocities. The results demonstrate that particle dispersion in plane wakes can produce highly organized patterns of particle concentrations. The particles at intermediate Stokes number are focused into sheet-like regions near the boundaries of the large scale vortex structures. In addition the spatial dispersion of the intermediate Stokes number particles was much larger than the smaller Stokes number particles. These experimental results strongly support previous numerical simulation findings.

Keywords: Particle dispersion; Plane wakes; Vortex structures; Stokes number; Digital image analysis

1. Introduction

A substantial amount of experimental and numerical evidence is presently available concerning the importance of vortex structures in the dispersion of solid particles in two types

* Corresponding author. Tel.: +1-509-335-3214; fax: +1-509-335-4662.
E-mail address: crowe@mme.wsu.edu (C.T. Crowe).

0301-9322/00/$ - see front matter
PII: S0301-9322(99)00105-6

of free shear flows, plane mixing layers and axisymmetric jets. Particle dispersion by vortex structures in plane mixing layers has been investigated both experimentally and numerically by Wen et al. (1992) and experimentally by Lazaro and Lasheras (1989, 1992a, 1992b); particle dispersion in axisymmetric jets has been investigated numerically by Chung and Troutt (1988) and experimentally by Longmire and Eaton (1992). Reviews concerning these results and other investigations can be found in Crowe et al. (1988, 1993, 1995). For both mixing layers and axisymmetric jets (upstream of the end of the potential core region) the large scale vortex dynamics are dominated by pairing interactions between vortex structures of the same sign. However, for a third class of basic free shear flows, plane wakes, large scale vortex pairings are much less a characteristic feature since the flow is typically composed of an alternating arrangement of opposite sign vortex structures (Huerre and Monkewitz, 1990). It is therefore quite plausible that the particle dispersion character in wake flows may be significantly different from that observed in mixing layers and jets. A recent two-dimensional (2D) numerical simulation by Tang et al. (1992) does indeed indicate that the dispersion of particles in a plane wake may even be more organized for intermediate Stokes number particles than that observed previously in mixing layers and axisymmetric jets.

The global influence of vortex structures on the particle dispersion process for situations where the material density of the particles is high compared to the fluid density, the particle diameters are small compared to the flow length scales and the particle Reynolds numbers are small is for many typical applications primarily dependent on the particle Stokes number. This result is not surprising since the general small particle motion equation developed by Maxey and Riley (1983) may be reasonably approximated by a simple Stokes drag relation under these restrictions (see also Chung and Troutt, 1988). Specifically the applicable non-dimensional particle motion equation, including gravitational effects, becomes

$$\frac{\mathrm{d}\vec{V}_\mathrm{p}}{\mathrm{d}t} = \frac{f}{St}\left(\vec{V} - \vec{V}_\mathrm{p}\right) + \frac{\hat{g}}{Fr}$$

where $\vec{V}_\mathrm{p}$ is the non-dimensional particle velocity, $\vec{V}$ is the non-dimensional flow velocity, t is the non-dimensional time, $\hat{g}$ is a unit vector in the direction of the gravitational acceleration, St is the Stokes number, Fr is the Froude number and f is a factor for modifying the Stokes drag over a range of Reynolds numbers. From experimental results f can be approximated by $f = 1 + 0.15Re_\mathrm{p}^{2/3}$ where Re_p is the particle Reynolds number based on the relative velocity magnitude $|\vec{V} - \vec{V}_\mathrm{p}|$ and particle diameter. This relation is applicable for $Re_\mathrm{p} < 1000$. The Stokes number in this relation is defined as $\tau_\mathrm{a}/\tau_\mathrm{f}$ where τ_a is the particle aerodynamic response time and τ_f is a characteristic time associated with the large scale flow structures. The particle aerodynamic response time is defined as $\tau_\mathrm{a} = \frac{\rho_\mathrm{p} d_\mathrm{p}^2}{18\mu}$, where ρ_p is the particle material density, d_p is the particle diameter, and μ is the fluid viscosity. The characteristic flow time is obtained from a flow length scale, L, divided by a characteristic velocity U_0. The Froude number is defined as U_0^2/gL where g is the gravitational acceleration. For terrestrial flows with relatively high characteristic velocities the reciprocal Froude number term is small and typically neglected.

This leaves only the Stokes drag term on the right side of the particle motion equation. The reasonableness of this approximation is however strictly dependent on the relative values of the Stokes number and the Froude number. For relatively large Stokes number particles

gravitational effects cannot be neglected. The importance of the Stokes number in the particle dispersion process in free shear layers has been discussed previously (Crowe et al., 1988, 1993, 1995). Particularly interesting has been the behavior of particles at intermediate Stokes numbers which may produce dispersion rates much greater than fluid tracer elements. The particle dispersion patterns at these Stokes numbers may also exhibit a remarkable degree of organization.

One of the most striking examples concerning the self-organization of intermediate Stokes number particles, as mentioned previously, was recently observed in a numerical simulation of a plane wake flow (Tang et al., 1992). This 2D discrete vortex simulation of the dispersion process in a plane wake produced by a thick trailing edge shows that particles with Stokes numbers near unity are focused into extremely thin regions near the outer edges of the vortex structures. (The Stokes number for the wake flow particles is based on a fluid time scale involving the bluff body half thickness and the free stream velocity). The counter rotating large scale vortices produced by the plane wake tend to inhibit the vortex pairing process. The stable arrangement of the counter rotating vortices is apparently an important factor for producing the high degree of organization observed in the wake flow particle dispersion patterns at intermediate Stokes numbers.

The major objective of the investigation discussed here is to provide independent qualitative and quantitative experimental data concerning plane wake particle dispersion. The experiments are limited to solid particles at intermediate and small Stokes number conditions, since gravitational effects become dominant for particles with large Stokes numbers. However, the results do show substantial differences in the dispersion patterns between the small and intermediate Stokes number particles.

2. Experimental facilities and techniques

An open return wind tunnel facility with a cross section of 46×61 cm and of length 198 cm was used for the experiments described here. Details concerning this facility are described by Wen et al. (1992). The mean flow uniformity produced by this wind tunnel is within $\pm 1.0\%$ with free stream turbulence intensity levels of order 0.1%. A square end splitter plate with a trailing edge thickness of 31.5 mm was used to produce the investigated wake flow. The free stream velocity for the wake experiments was nominally 3.3 m/s. The trailing edge boundary layers on the splitter plate were laminar with a momentum thickness of approximately 1 mm. Fig. 1 shows a schematic of the test section arrangements.

To control the phase of the wake vortex shedding process a high power low frequency loudspeaker system driven by a Hewlett Packard 201c audio oscillator and 50 W Dynaco audio amplifier was employed. The effective frequency range of the loudspeaker system was 20–200 Hz. Nominal sound pressure levels of 90–92 dB were produced by this system at the plate trailing edge under typical forcing conditions. The loudspeaker was located on the top wall of the test facility directly above the trailing edge of the square end splitter plate.

Acoustic forcing techniques typically couple with low speed flows most effectively in the generation region of the free shear flow near the trailing edge of the bluff body. Crighton (1981) article discusses the acoustic coupling process with free shear flows in detail. Acoustic

forcing techniques of this type are commonly used to control the initiation and later development of large scale structures in free shear layers (Ho and Huerre, 1984). These techniques may be most effective for controlling free shear flows which are of the convective instability type such as plane mixing layers. Wakes from bluff bodies (with large ratios of bluff body thickness to trailing edge boundary layer thickness), however, may produce absolute type instabilities (Huerre and Monkewitz, 1990; Yang et al., 1992) which may be less susceptible to controlled forcing. Huerre and Monkewitz (1990) give an extensive review concerning the characteristics of absolute and convective instabilities in various flows. It was found, however, in this experimental wake flow that some degree of control of the vortex shedding phase and frequency could be accomplished using acoustic forcing techniques. This finding is similar to that observed by Lotfy and Rockwell (1993) in their oscillating trailing wake experiments.

The particles used in the dispersion experiments were solid glass beads of density 2.4 g/cm^3. Particles with nominal diameters of 10 and 30 μm with ±20% standard deviation in diameter were used for the dispersion experiments. The two nominal particle sizes have associated Stokes number based on the free stream velocity and the half width of the plate trailing edge of $0.15 \pm 44\%$ and $1.4 \pm 44\%$. The glass bead particles were injected into the wake flow from the centerline of the base of the plate trailing edge through a 3.175 mm diameter hole. The particle injection rates were kept at a low value of.08 g/s to reduce the possibility of significant coupling effects on the flow from the presence of the particles. The particles were supplied to the trailing edge orifice from a fluidized bed particle supply system described by Wen et al. (1992). The particles were injected at a downstream velocity of approximately 0.5 m/s. This particle velocity matches closely the measured time average air velocity at $x/s = 0.4$ on the

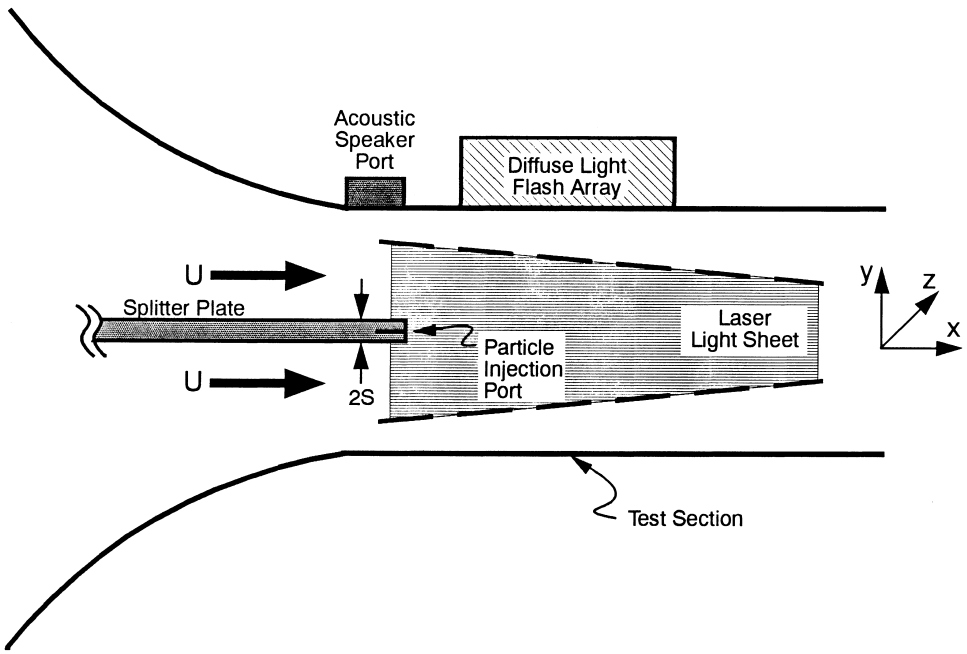

Fig. 1. Schematic of test facility.

wake centerline. This particle injection velocity therefore insures that the particles will be initially in dynamic equilibrium with the mean air flow.

In addition to the solid particle dispersion experiments smoke streaklines generated by a smoke wire technique (Corke et al., 1977) were used to visualize the instantaneous flowfield. The smoke particles generated from the smoke-wire technique are estimated to be of the order of 1 μm or less in diameter which gives an approximate particle Stokes number of the order of 10^{-3}. Particles at this Stokes number should be expected to closely approximate neutral flow tracers (Crowe et al., 1988).

The primary particle dispersion measurement approach in this research employed visualization techniques to acquire instantaneous photographic images of the dispersion patterns. The images were analyzed using digital techniques to identify, locate and count particles. Computerized numerical and graphical techniques could then be employed to quantify and display the results. This general approach has previously been successfully applied to investigate the particle dispersion process in an axisymmetric jet by Longmire and Eaton (1992).

Illumination of the glass bead particles was obtained using a 20 W pulsed copper-vapor laser. The laser beam under normal operating conditions pulsed at 6000 Hz. The laser light beam was converted from a 20 mm diameter circular cross section to an approximately 2 mm thick sheet over the two-phase flow region of interest with an optical system employing a 2 m focal length convex spherical lens and a 300 mm focal length convex cylindrical lens. These lenses produce a light sheet parallel to the streamwise direction (x dimension), which is gradually diverging in cross stream width (y dimension) while gradually converging then diverging in spanwise thickness (z dimension) over the measurement region. The optical arrangement for the laser light sheet is shown in Fig. 2. In addition to the laser sheet light experiments a bank of 4 high voltage flash units were used to provide illumination for the smoke wire flow visualization experiments. The duration of each laser pulse for the copper vapor laser is of the order of 30 ns. The exposure time for the high voltage flash units was approximately 0.1 ms. The photographic images were acquired with an electronic motor driven 35 mm camera.

To obtain images illuminated by a designated number of laser pulses at a particular phase in the vortex shedding process, the laser and the camera shutter operation must be synchronized through the use of an electronic controller which is also capable of monitoring a reference signal associated with the state of the flow field. This rather exacting set of requirements was successfully accomplished using a micro-computer based system with associated A/D converter, timing controller and triggering circuit. A schematic of the digital control system and associated electronics is shown in Fig. 3. Details concerning the timing sequencing software and hardware and the operation of this system can be found in Yang (1993).

Single pulse photographs obtained at selected phases of the forcing signal were then developed and printed on 8×10 photographic sheets. These printed photographs were transformed into digital images by a HP Scanjet IIC scanner interfaced with a NeXT microcomputer with a linear spatial resolution of 7 pixel lengths per mm. Software was then employed to convert the gray scale images into binary images, (all pixels either on or off). The centroid, area and moment of inertia of each digital object associated with a contiguous group of 'on' pixels was computed to determine the number of particles in an object according to

specific criteria in a fashion similar to that discussed by Longmire and Eaton (1992). Because of diffraction effects, a typical particle image would cover an area of the order of 10 square pixels. The particle number and centroid of each object were used to construct a 2D particle number density map. Square cells of 8×8 pixels were employed to set up the grid system for the number density map. The particle number assigned to each of the grid points encompassing

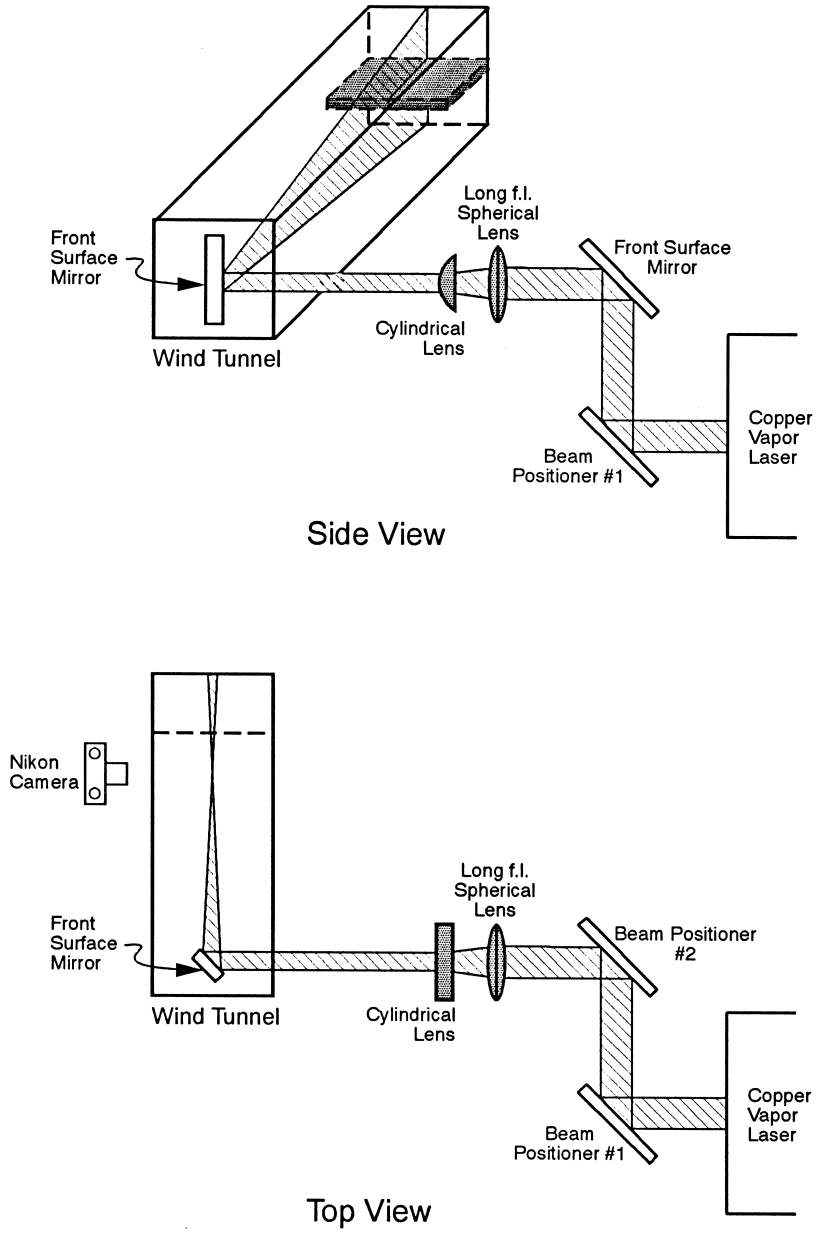

Fig. 2. Optical arrangement for laser sheet flow visualization.

an object was apportioned according to the position of the object centroid with respect to the nearest grid points. The number density maps were then normalized by the total number of particles counted. A typical particle map involves several thousand particles covering a rectangular experimental spatial area of approximately 5 × 10 cm. Additional details concerning the digital image processing techniques can be found in Yang (1993).

The velocities of individual particles were measured using particle tracking techniques. Closely spaced multiple particle images were obtained with illumination from controlled laser pulses. Photographs with six sequential laser pulses were processed by digital image analysis software to determine the approximate particle velocities by measuring the displacement of particle images during the elapsed time (160 μs) between pulses. The computations for the particle number density and the particle velocity measurements were carried out on a Dec5000 workstation. Details concerning the software developed are discussed in Yang (1993).

The single phase air velocity was measured using a calibrated single-wire Dantec P11 hot-wire probe mounted with the wire aligned in the spanwise direction. A Dantec 5613 constant temperature anemometer was used to acquire the signals. The output from the anemometer was then filtered and digitized following standard data acquisition techniques (details can be found in Yang (1993)). The hot-wire response is assumed to be primarily related to the

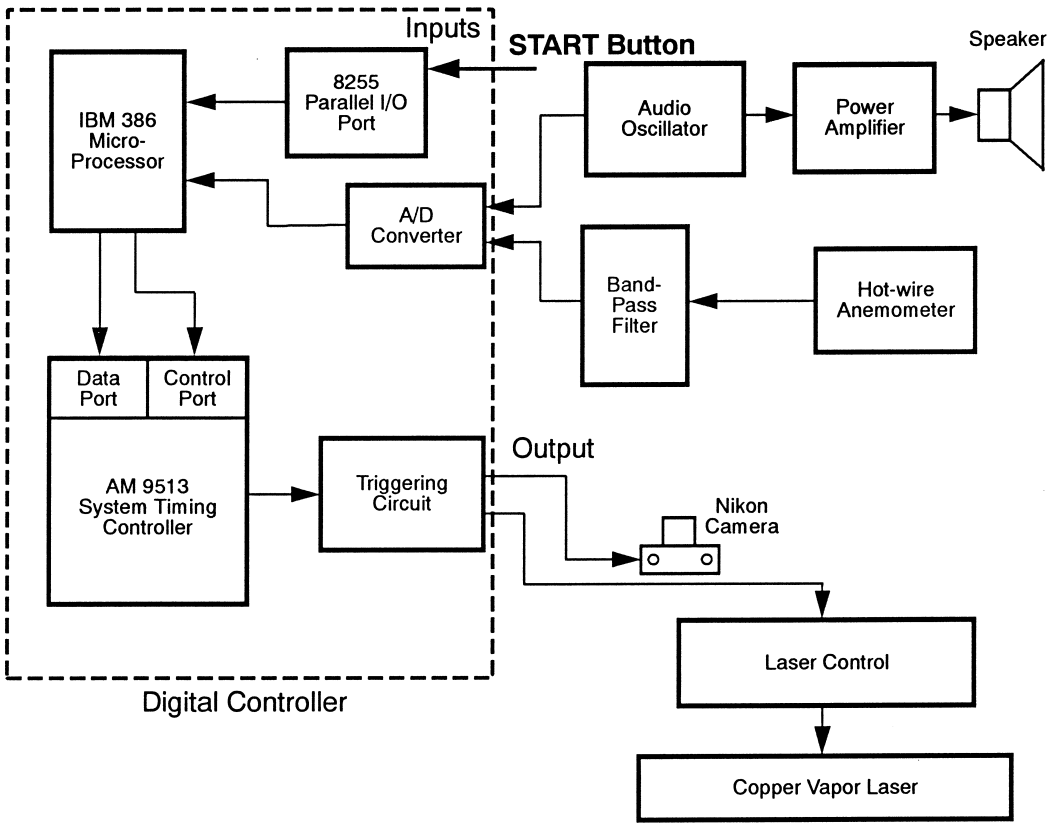

Fig. 3. Schematic of the digital control system.

streamwise velocity component for all measurements presented in this paper. However, some measurements from the region immediately downstream of the bluff body ($x/s = 0.4$) were omitted because the high turbulence levels encountered there might affect hot-wire accuracy.

3. Experimental results

3.1. Wake flow

Time averaged velocity defect profiles of the wake flow at downstream positions x/s of 0.4, 8 and 12 (where s is the half width of the plate trailing edge) are shown in Fig. 4 for a free stream velocity U_∞ of 3.3 m/s. The associated Reynolds number is 6500 based on the trailing edge thickness and free stream velocity. The velocity measurements are presented in non-dimensional form as $\tilde{U} = (U_\infty - U)/(U_\infty - U_{cl})$ where U is the local mean velocity and U_{cl} is the mean velocity at the center of the wake. An experimental curve fit obtained by Wygnanski et al. (1986) for the self-similar far wake flow given by

$$\tilde{U} = \exp\left(-0.637\eta^2 - 0.056\eta^4\right)$$

where, η is the cross-stream coordinate normalized by the wake half width is also shown on the same graph. Estimated errors associated with individual dimensional velocity measurements are of the order of $\pm 2\%$ of the free stream velocity. Uncertainties associated with $\tilde{U}$ are somewhat larger since this quantity involves velocity differences.

The results from the mean velocity measurements demonstrate a typical near wake flow development. An initial approximately square cornered velocity defect profile relatively quickly develops into a more rounded wake profile by $x/s = 8.0$, and continues to change towards the self-similar profile of a far wake with downstream position.

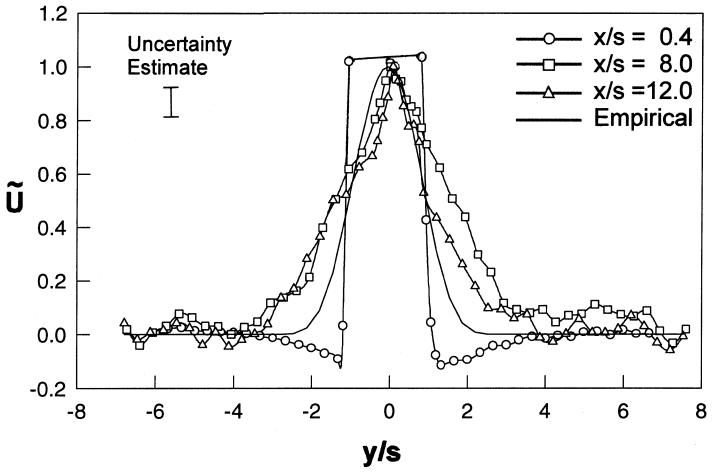

Fig. 4. Time averaged streamwise velocity defect profiles.

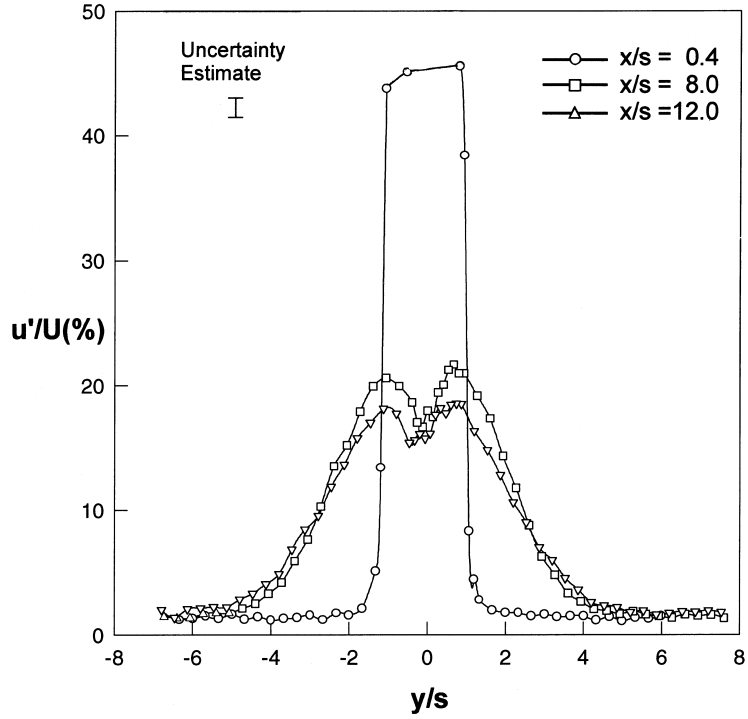

Fig. 5. Time averaged streamwise turbulence intensity profiles.

Time averaged downstream turbulence intensity levels are shown in Fig. 5 for positions $x/s = 0.4$, 8 and 12. The levels of turbulence intensity at $x/s = 0.4$ are quite high relative to nominal levels in turbulent free shear flows. These high levels of turbulence intensity are commonly observed in recirculating separation regions near the downstream edge of bluff bodies. As discussed in previous reported investigations concerning single sensor hot-wire measurements in separated flows (Troutt et al., 1984), turbulence intensity levels above 35% are probably somewhat inaccurate. This is produced by the inability of the single-sensor hot-wire to distinguish between positive and negative flow fluctuations in the downstream direction. We have therefore omitted measured hot-wire results from the central wake region at $x/s = 0.4$. Maximum turbulence intensity levels near the center line of the wake at downstream positions of $x/s = 8$ and 12 are in 15–20% range which are typical of plane wake flows (Wygnanski et al., 1986). The turbulence intensity profiles also exhibit a typical bimodal character indicative of the cross-stream spatial separation between opposite sign vortex streets produced by each side of the splitter plate (Wygnanski et al., 1986).

Typical photographic images of instantaneous streaklines from the non-forced and forced wake flow obtained from the diffuse light smoke wire visualization technique are shown in Fig. 6. The organized large scale vortex structures of alternating sign produced by the wake are quite obvious in these streakline visualizations. In addition, the forcing appears to have little effect on the large scale structures. Hot-wire velocity results involving mean flow, turbulence intensity levels, and spectral measurements also support this lack of significant effect of the

acoustic forcing on the character of the large scale flow structures and the time average flow field (Yang, 1993). The spatial extent of this photograph covers the initial region of the wake development ($0 < \frac{x}{s} < 11$, $-3 < \frac{y}{s} < +3$), where x is the downstream position from the plate trailing edge and y is the cross-stream position measured from the wake centerline. The forcing frequency was selected to correspond to the naturally occurring vortex shedding frequency. The vortex shedding frequency was measured by hot-wire anemometry to be at a Strouhal number of 0.26 based on trailing edge thickness and free stream velocity.

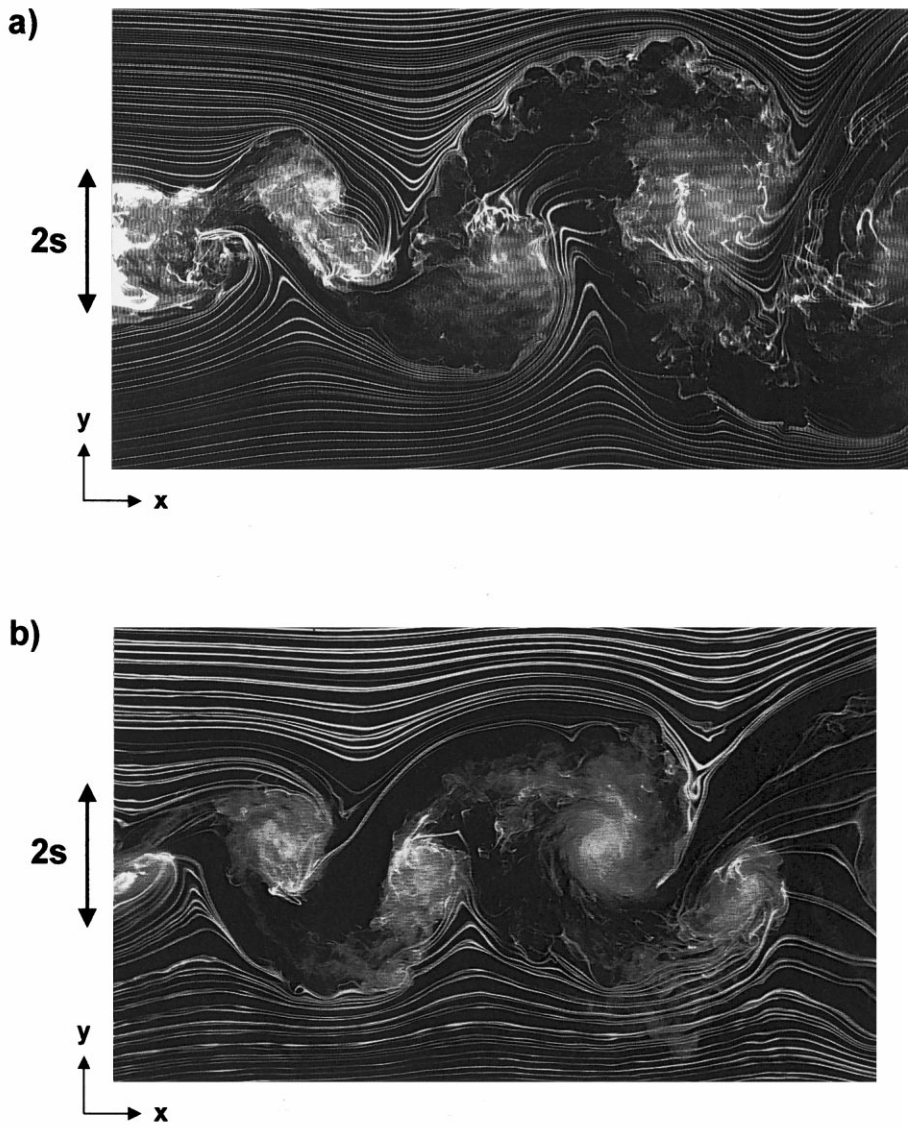

Fig. 6. Typical instantaneous streakline patterns of near wake flow: (a) nonforced, (b) forced at natural vortex shedding frequency ($St = 0.26$).

To determine whether external forcing could provide an effective phase lock to the vortex shedding processes, phase average streamwise velocity measurements were carried out. The phase average velocities were obtained by averaging values at selected phases, ϕ, which are each separated by increments of 10° based on the period of the acoustic forcing signal. Each selected phase result was then averaged over 1000 samples. The phase average results are presented as a normalized velocity, U^*, defined as:

$$U^* = \frac{U_\infty - \langle U \rangle}{U_\infty}$$

where $\langle U \rangle$ is the phase average velocity. Fig. 7 shows the phase average velocity results obtained from $x/s = 12$ at various cross-stream positions. Fig. 7(a) shows results from near the central region of the wake where the large scale vortices have oscillations that are sinuous in nature with a period identical to the forcing signal. In addition the oscillations at $y/s = \pm 1$ are 180° out of phase with each other demonstrating the alternating character of the vortices on

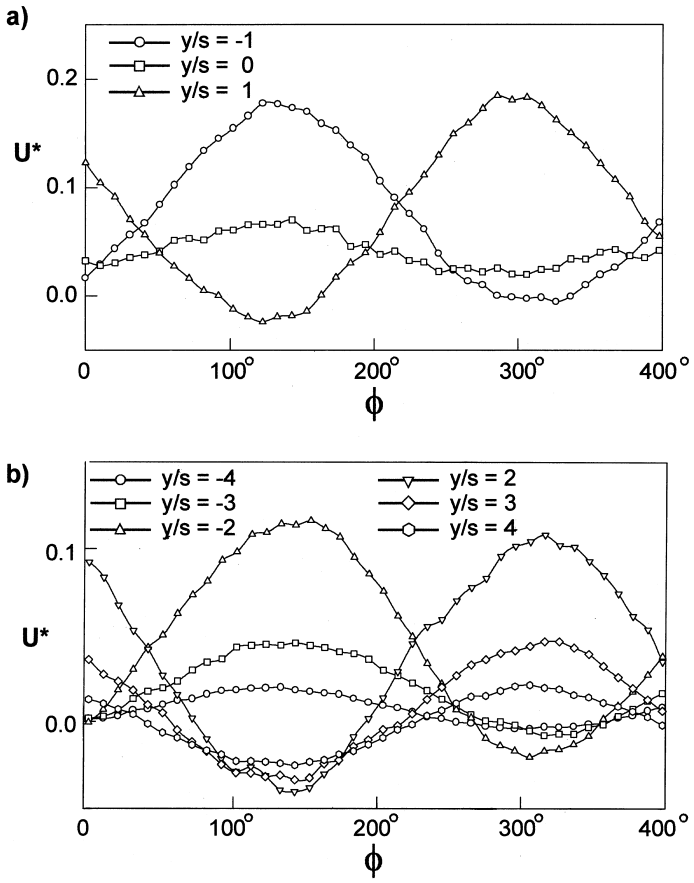

Fig. 7. Phase average streamwise velocity defect, U^*, as a function of phase, ϕ, at various cross stream positions obtained at $x/s = 12$. (a) $y/s = 0, \pm 1$, (b) $y/s = \pm 2, \pm 3, \pm 4$.

each side of the wake. The amplitude of the oscillation in U^* decreases somewhat at the center of the wake, probably because vortices of different signs from both sides of the wake are influencing the velocity levels. The oscillation amplitude of U^* also decreases steadily with cross stream distance away from the center of the vortices as shown in Fig. 7(b) for measurements from $y/s = \pm 2, \pm 3, \pm 4$. These results demonstrate that forcing at the natural vortex shedding frequency creates a significant degree of phase locking in the vortex shedding process.

Phase average velocity defect profiles obtained at $x/s = 8$ at selected phases are shown in Fig. 8(a). The results show a shifting of the maximum velocity defect from negative to positive values of y/s as the phase is shifted through more than a half period of the forcing signal. The maximum velocity defect position is strongly affected by the presence of the large scale vortices and the phase averaging at selected phases is apparently capable of locking onto the upper or lower vortex presence. Profiles of the phase average velocity defect at $x/s = 12$ are shown in Fig. 8(b) at three relative phases. The profiles demonstrate a character similar to the $x/s = 8$ profiles with the velocity defect peak shifting from below the wake centerline to above the

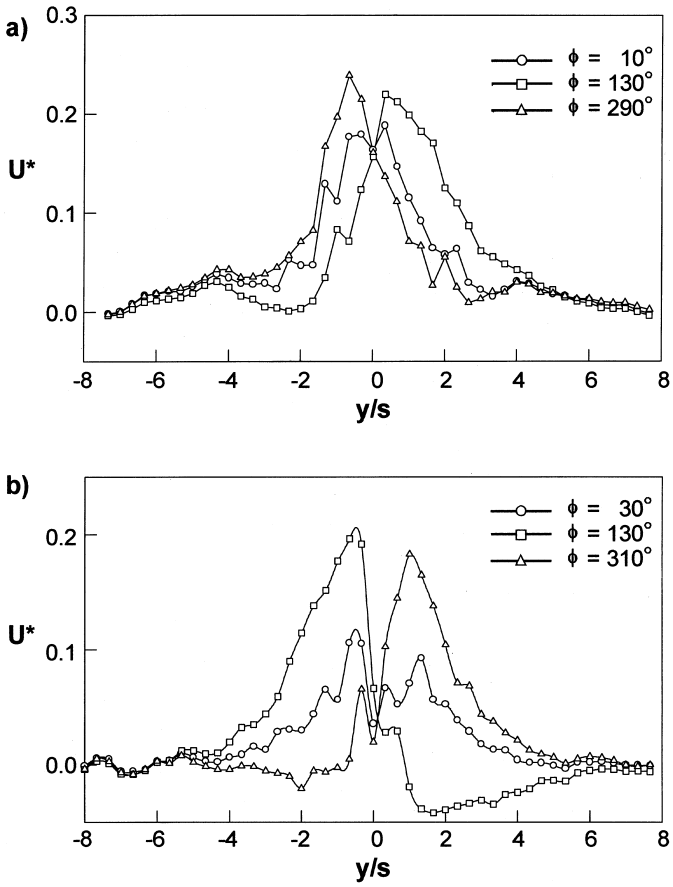

Fig. 8. Phase average streamwise velocity defect profiles (a) $x/s = 8$, (b) $x/s = 12$.

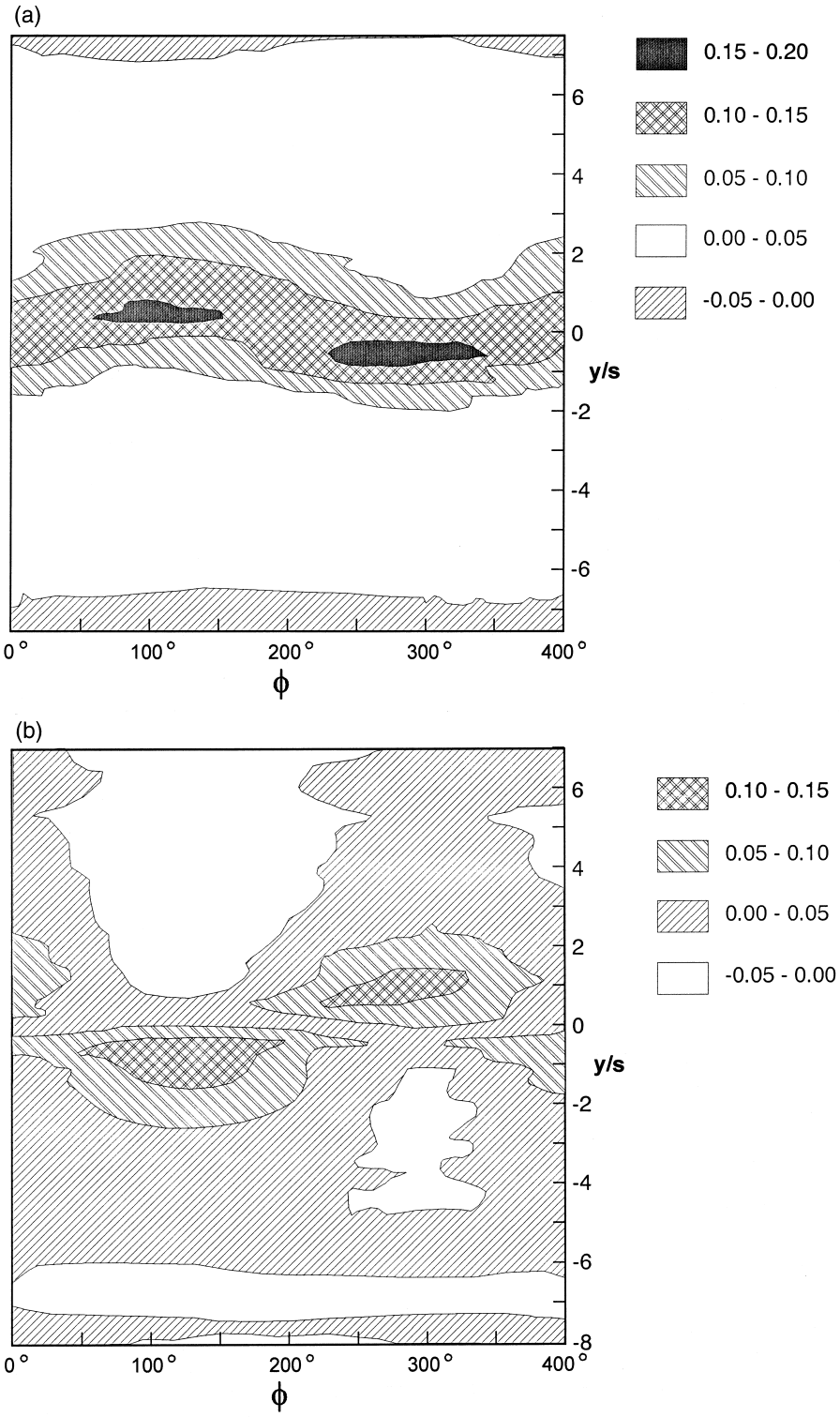

Fig. 9. Contour plot of phase average streamwise velocity defect (a) $x/s = 8$, (b) $x/s = 12$.

centerline with changes in phase angle. The maximum values of phase averaged velocity defect are about twice that of the time average velocity defect.

Contour plots of phase average U^* measurements at $x/s = 8$ and 12 are presented in Fig. 9. These plots demonstrate the alternating peak nature of the velocity defect regions associated with convecting vortex structures.

A three-dimensional (3D) view $x/s = 12$ of the cross-stream gradient of the velocity ($\frac{\partial U^*}{\partial \eta}$), which is associated with the spanwise vorticity, is shown in Fig. 10. A definite trend appears with positive values of $\frac{\partial U^*}{\partial \eta}$, indicating levels of spanwise (z) vorticity dominating at positive values of y/s. Similarly, negative values of $\frac{\partial U^*}{\partial \eta}$, indicating negative vorticity, tend to dominate at negative values of y/s. More extensive techniques for visualizing and identifying 3D vortex structures can be found in Soria and Cantwell (1994).

3.2. Flow and particle visualization studies

Instantaneous particle dispersion images obtained from laser sheet illumination for three selected relative phase angles are shown in Figs. 11 and 12 for the nominal $St = 0.15$ particles. To improve resolution levels the photographs cover a limited downstream spatial region ($5 \leq x/s \leq 14$; $-3.5 \leq y/s \leq 3.5$). For every selected phase angle the particle concentration or number density levels for these relatively small particles appear to take on maximum values within the central region of the vortex structures.

Instantaneous particle dispersion images at the three selected phase angles for the nominal $St = 1.4$ particles are shown in Fig. 13. The images obtained from these larger particles display a significantly different pattern from those observed with the smaller particles. The larger

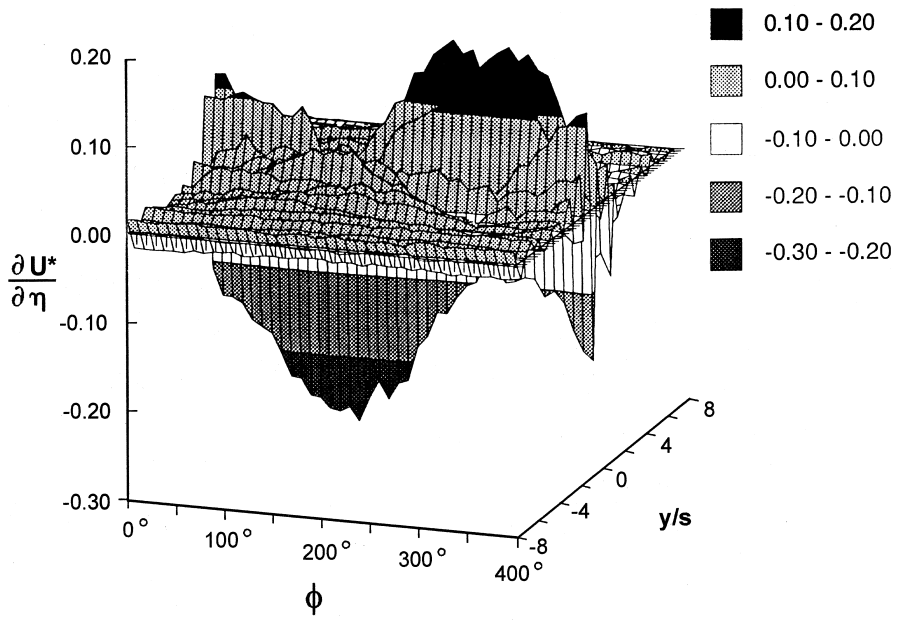

Fig. 10. Perspective view of the 3D phase average streamwise velocity gradient $\frac{\partial U^*}{\partial \eta}$ profiles at $x/s = 12$.

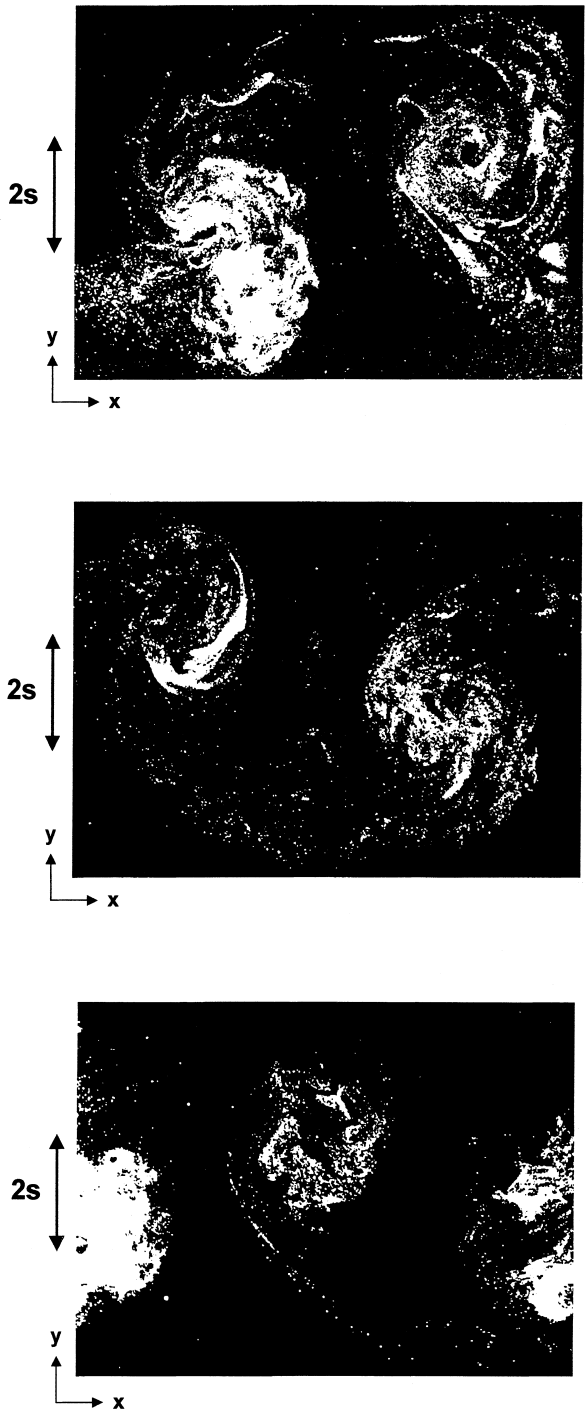

Fig. 11. Instantaneous planar (x–y) dispersion patterns of 10 μm particles at three sequential phase angles. (a) $\phi_1 = 0° \pm 4°$, (b) $\phi_2 = 140° \pm 4°$, (c) $\phi_3 = 220° \pm 4°$.

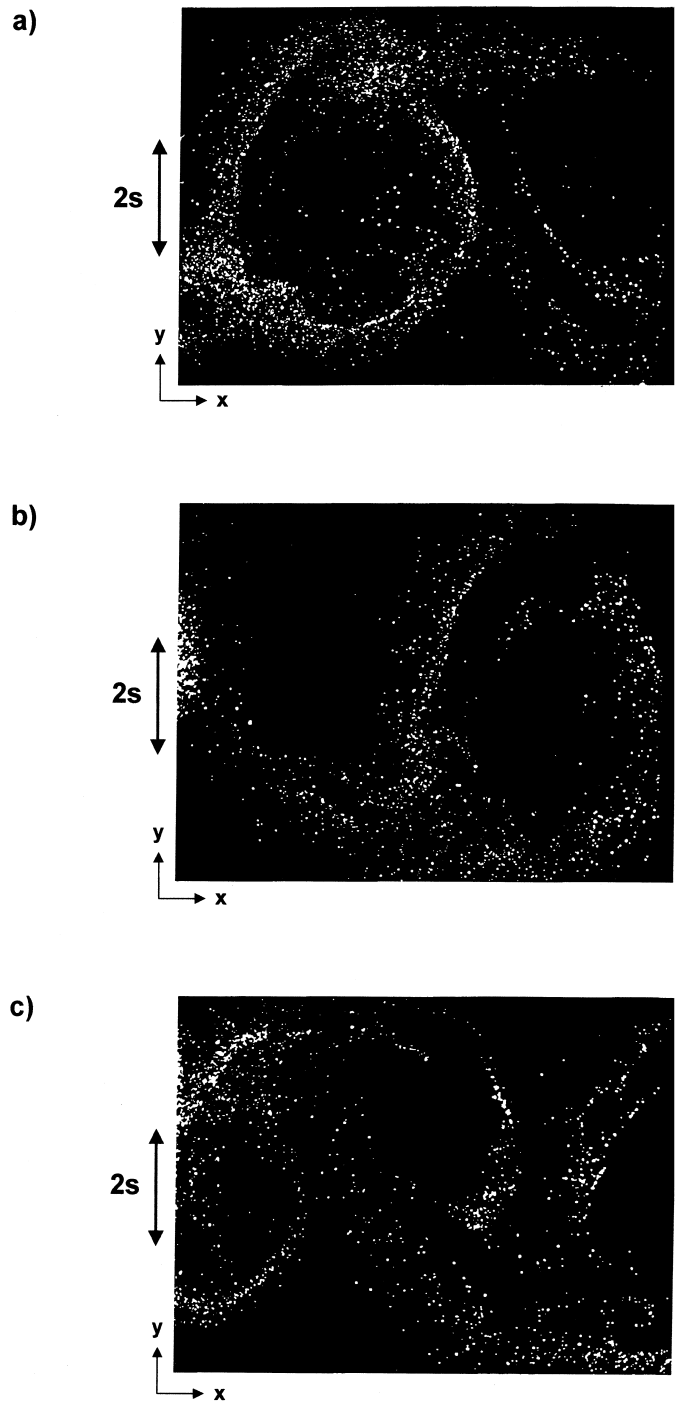

Fig. 12. Instantaneous planar (x–y) dispersion pattern of 30 μm particles at three sequential phase angles. (a) $\phi_1 = 0^\circ \pm 4^\circ$, (b) $\phi_2 = 140^\circ \pm 4^\circ$, (c) $\phi_3 = 220^\circ \pm 4^\circ$.

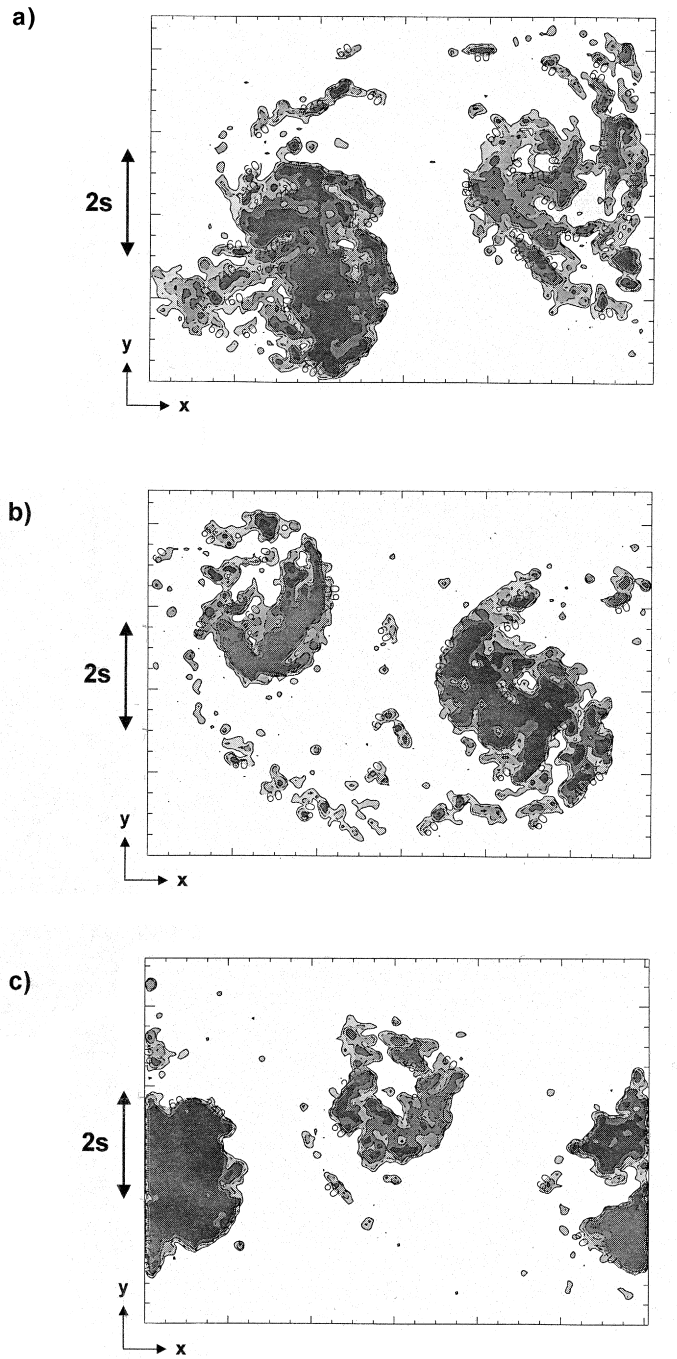

Fig. 13. Instantaneous number density maps of 10 μm particles at three sequential phase angles. $St = 0.15$. (a) $\phi_1 = 0^\circ \pm 4^\circ$, (b) $\phi_2 = 140^\circ \pm 4^\circ$, (c) $\phi_3 = 220^\circ \pm 4^\circ$.

particles congregate densely in thin bands near the outer boundaries of the vortex structures. The general features of the dispersion patterns from both the small and intermediate Stokes number particles appear to be in close general agreement with previous numerical simulation results (Tang et al., 1992). Direct comparisons with numerical particle dispersion results are shown later.

Particle concentration or number density maps were obtained from the instantaneous phase locked images using image analysis techniques. The results for the Stokes number 0.15 particles are shown in Fig. 13. The particle concentration levels are divided into four gray scales with each gray scale representing a two-fold increase in concentration. In general particle concentration levels are highest near the central regions of the vortex structures, however, local banded concentration regions within the structures are also apparent. High particle concentration regions are also apparent in bands connecting the large scale structures. These banded concentration regions were also observed for small Stokes number particles in previous numerical simulation studies (Tang et al., 1992).

Concentration maps for the $St = 1.4$ particles at three selected phase angles are shown in Fig. 14. For the larger particles the maps quantify the high levels of particle concentration near the outer boundary regions of the large scale vortex structures and the extremely low concentration levels throughout the central region of the structures. This experimental result is in close agreement with previous numerical simulation studies (Tang et al., 1992). In addition, particle accumulation in the rib or saddle region between the adjoining vortex structures are also apparent.

Typical multiple exposure images of the particles used for obtaining particle velocity information are shown in Fig. 15 for both particle sizes. Six consecutive laser pulses were employed for each image. Each laser pulse was separated in time by 1/6000 a second for optimal velocity resolution and particle identification. Only those particles with clearly distinguishable consecutive images were used for the velocity computations. All other particle streaks that were incomplete or not clearly recognizable were discarded.

Particle velocities derived from the multiple exposure images are shown in Fig. 16 at two selected phase angles for the $St = 0.15$ particles. The free stream velocity has been numerically subtracted from the computed particle velocity to more clearly illustrate the particle motion associated with the vortex structures. Near the central region of the vortex structures the small particles tend to acquire velocity vectors which are aligned approximately along an azimuthal coordinate centered on the vortex structures. The direction of the azimuthal particle trajectories changes from clockwise to counterclockwise with each sequential vortex structure. The magnitude of the particle velocities also tends to decrease as distance from the vortex centers increase, demonstrating that as the particles move away from the vortex centers they approach dynamic equilibrium with the velocity of the free stream air.

Particle velocities derived from the images for the $St = 1.4$ particles are shown in Fig. 17 at two selected phase angles. The velocity vectors for these larger particles do not, in general, map out closed circular patterns. Rather the particle velocity vectors in the immediate vicinity of the vortex cores in this case tend to have significant radial components. This effect can be seen most clearly by comparing particle velocity vectors from the different size particles in selected regions.

For the phase ϕ_1 result a region near $y/s = +1$ and $x/s = 12.5$ shows significantly more

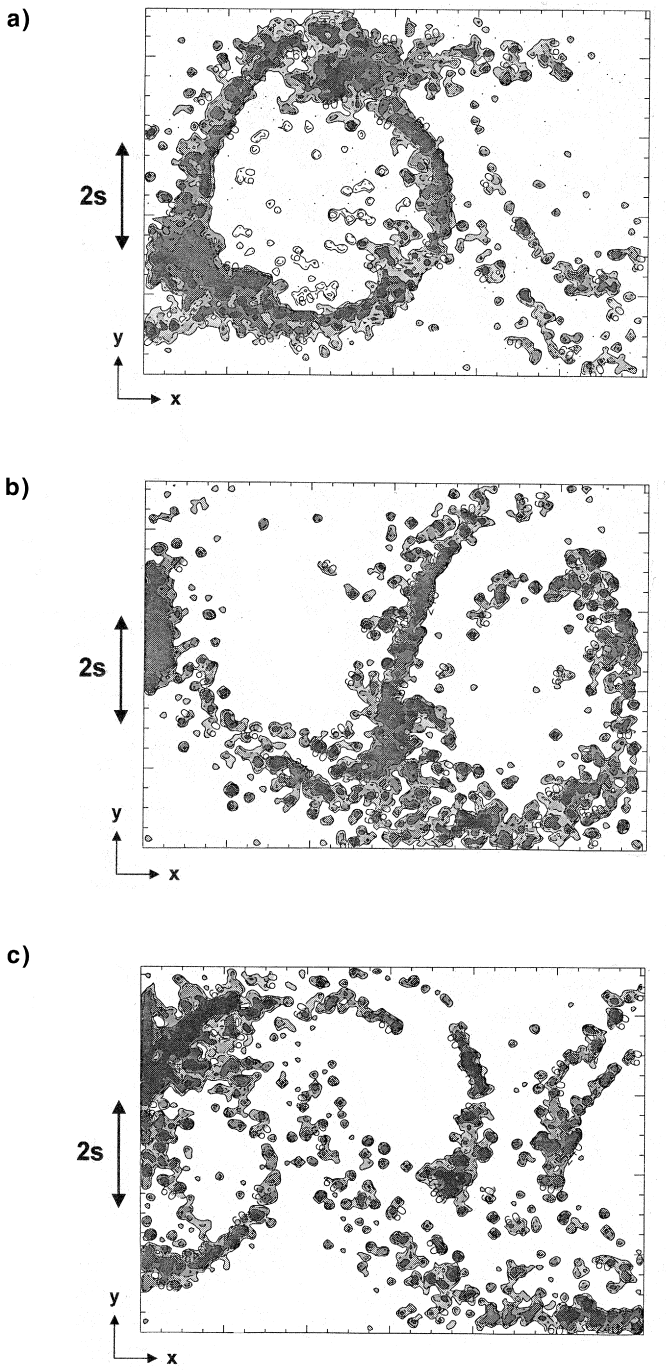

Fig. 14. Instantaneous number density maps of 30 μm particles at three sequential phase angles. $St = 1.4$. (a) $\phi_1 = 0^\circ \pm 4^\circ$, (b) $\phi_2 = 140^\circ \pm 4^\circ$, (c) $\phi_3 = 220^\circ \pm 4^\circ$.

cross stream (y) velocity component for the larger particles. For the phase ϕ_2 result a region near $x/s = 8$ and $y/s = +2$ also shows this effect. This additional cross stream or radial component produces particle streamlines with an outward spiral character near the vortex cores. Beyond the outer boundaries of the vortices the larger particles also approach dynamic equilibrium with the velocity of the free stream. The net result of this particle movement is the preferential accumulation of the larger particles near the outer boundaries of the vortex structures and in regions between adjoining structures.

A direct quantitative comparison of the experimental results with previous numerical simulation results (Tang et al., 1992) can be obtained by computing the crosstream particle dispersion measure defined as $D = (1/N)[\sum_1^N (y_i - y_{i_0})^2]^{1/2}$ for the two Stokes number particles, where N is the total number of particles considered, y_{i_0} is the ith particle's initial y position and y_i is the ith particle's present y position. For this computation all particles were assumed to initiate from the wake centerline. Tang et al. (1992) previous numerical results of the particle dispersion measure were presented as normalized by the dispersion of fluid tracer

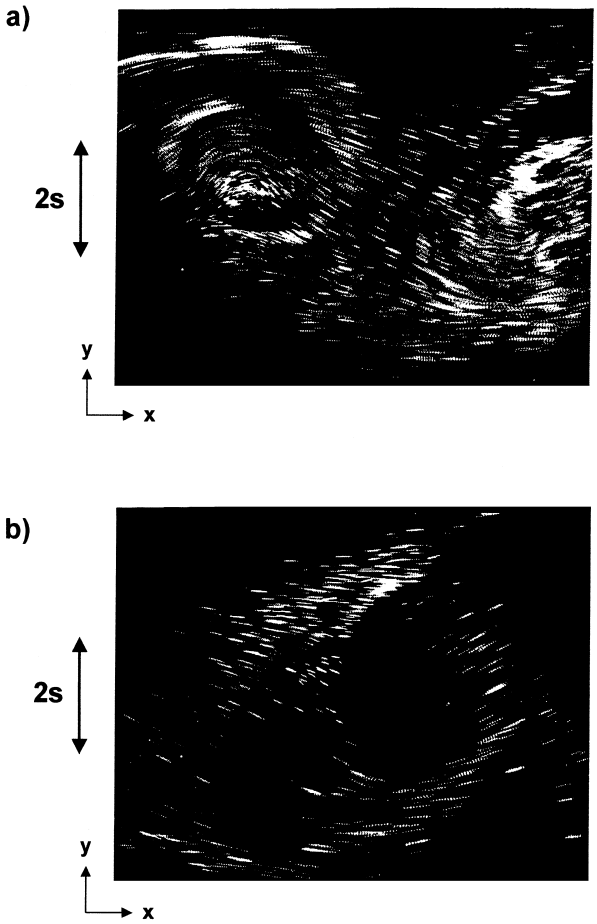

Fig. 15. Multiple-exposure images for particle velocity measurements. (a) 10 μm particles, (b) 30 μm articles.

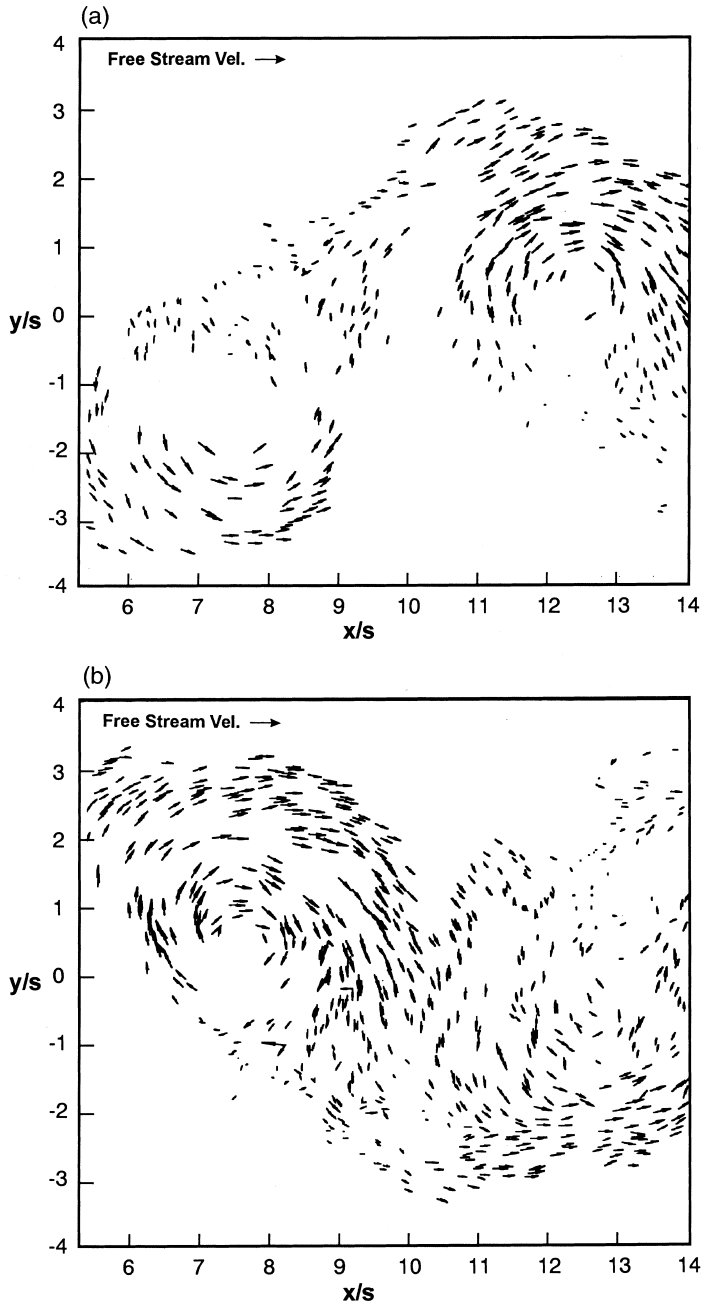

Fig. 16. Instantaneous particle velocity maps of 10 μm particles at two phase angles. (a) $\phi_1 = 0^\circ \pm 4^\circ$, (b) $\phi_2 = 140^\circ \pm 4^\circ$.

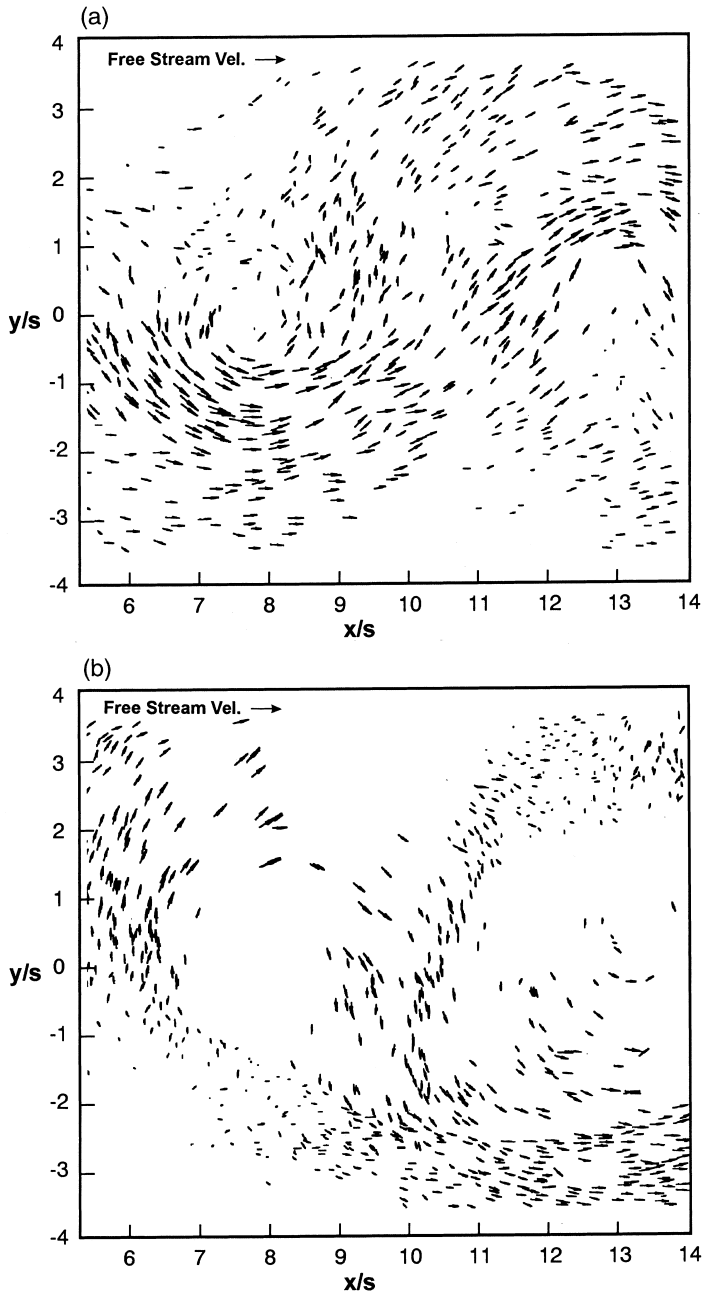

Fig. 17. Instantaneous particle velocity maps of 30 μm particles at two phase angles. (a) $\phi_1 = 0° \pm 4°$, (b) $\phi_2 = 140° \pm 4°$.

Table 1
Dispersion ratio between Stokes numbers $1.4 \pm 44\%$ and $0.15 \pm 44\%$

Experimental	Dispersion ratio
ϕ_1 average	1.47
ϕ_2 average	1.67
ϕ_3 average	1.54
Overall experimental average	1.56
Numerical result range	1.55–3.0

particles of vanishingly small Stokes number. The experimental results can be compared to the numerical results by computing the ratio of the dispersion values of the large Stokes number particles to the dispersion values of the small Stokes number particles. The dispersion ratios were then computed over an ensemble of realizations at each of the selected phases and finally an average over all phase results was computed.

The experimental particle dispersion ratio results from each phase average and the overall averaged results are shown in Table 1 as well as dispersion ratio results from a previous plane wake numerical simulation (Tang et al., 1992). The numerical result range was obtained by evaluating the simulated dispersion results over the range of particle Stokes numbers involved in the experiment. The higher value in the numerical range shown in the table was obtained from the simulated results by dividing the particle dispersion at $St = 1.4 + 44\%$ with the dispersion at $St = 0.15 - 44\%$. The lower value was obtained by dividing the particle dispersion at $St = 1.4 - 44\%$ with the dispersion at $St = 0.15 + 44\%$. The agreement between the experimental and numerical results is reasonable especially considering the assumptions involved in the discrete vortex numerical model such as absolute two-dimensionality, neglection of viscous effects on the carrier flow and the uncertainties inherent in a complex experiment of this type.

4. Conclusions

The experimental results shown in this work strongly support previous numerical simulations (Tang et al., 1992) concerning particle dispersion in a plane wake. The results quantitatively demonstrate that the extent of particle dispersion can be strongly dependent on the particle Stokes number and that intermediate Stokes number particles ($St = 1.4 \pm 44\%$) have cross stream dispersion levels significantly greater than smaller Stokes number particles ($St = 0.15 \pm 44\%$).

Specifically, the overall experimental cross-stream dispersion ratio results between intermediate and small Stokes number particles fall into the range predicted by previous numerical predictions (Tang et al., 1992). In addition to the quantitative particle dispersion comparisons, qualitative comparisons of the organization and nature of the experimental dispersion patterns also appear to closely match previous numerical simulation results.

Experimental velocity measurements of particles obtained by multi-exposure tracking techniques demonstrate that the smaller Stokes number particles tend to follow circular

trajectories around the large vortex structure centers. The larger Stokes number particles, however, tend to possess instantaneous velocity vectors with significant radial components when the particles are near the cores of the large scale vortex structures. This experimental finding also demonstrates the centrifuging effect the organized vortex structures produce in the dispersion of intermediate size particles.

When one combines the overall results from both previous numerical and the present experimental approaches, it becomes apparent that the plane wake flow particle mixing process can in reality result in surprisingly ordered particle dispersion patterns. The order associated with these patterns becomes most dramatic when the particle Stokes number is of $O(1)$. Particles in this Stokes number range have aerodynamic response times which are too slow to follow the small scale vortices in the flow. They do, however, feel the influence of the largest scale vortices which have flow time scales approximately equivalent to the particle response time. The particles, however, have a much larger material density than the fluid particles surrounding them and therefore experience a centrifuging effect which moves them away from the core of the large scale vortices. As these intermediate size particles move toward the outer boundaries of the large scale structures the curvature of the local flow reduces and the particles begin to follow the local flow pathlines which circulate around the convecting large scale vortices. If the particle response time is exactly matched to the characteristic time of the large scale vortices numerical simulations show that eventually the outer boundaries of these vortices become outlined by the particle positions.

Particles with Stokes numbers much less than one are able to respond to the smaller scale flow patterns and therefore become essentially flow tracers. The trajectories of these particles distribute themselves throughout the large scale vortex cores. Particles with Stokes numbers much greater than one conversely are little affected by the flow fluctuations at any scales and therefore simply move in the direction of their initial trajectories with only slight deviations.

Acknowledgements

The authors gratefully acknowledge the support of Department of Energy Grant DE-FG06-86ER13567 under the direction of Dr. Oscar Manley and equipment grant support from the National Science Foundation, Grants No. CBT-8506618 and CBT-8806525.

References

Chung, J.N., Troutt, T.R., 1988. Simulation of particle dispersion in an axisymmetric jet. J. of Fluid Mech 186, 199–222.

Corke, T., Koga, D., Doubka, R., Nagib, H., 1977. A new technique for introducing controlled sheets of smoke streaklines in wind tunnels. ICIASF Report.

Crighton, D.G., 1981. Acoustics as a branch of fluid mechanics. J. Fluid Mech 77, 397–413.

Crowe, C.T., Chung, J.N., Troutt, T.R., 1988. Particle mixing in free shear layers. Prog. Energy Combust. Sci 14, 171–194.

Crowe, C.T., Chung, J.N., Troutt, T.R., 1993. Particle dispersion by organized turbulent structures. In: Roco, M.C (Ed.), Particulate Two-Phase Flow. Butterworth–Heinemann, London, pp. 626–669.

Crowe, C.T., Chung, J.N., Troutt, T.R., 1995. Particle interaction with vortices. In: Green, S. (Ed.), Fluid Vortices. Kluwer Academic Publishers, Dordrecht, pp. 829–861 (Chapter 20).

Ho, C.M., Huerre, P., 1984. Perturbed free shear layers. Ann. Rev. Fluid Mech 16, 365.

Huerre, P., Monkewitz, P.A., 1990. Local and global instabilities in spatially developing flows. Ann. Rev. Fluid Mech 22, 473.

Lazaro, B.J., Lasheras, J.C., 1989. Particle dispersion in a turbulent plane shear layer. Phys. Fluids A.1 (6), 1035–1044.

Lazaro, B.J., Lasheras, J.C., 1992a. Particle dispersion in the developing free shear layer. Part I: unforced flow. J. Fluid Mech 235, 143–178.

Lazaro, B.J., Lasheras, J.C., 1992b. Particle dispersion in the developing free shear layer. Part II: forced flow. J. Fluid Mech 235, 179–221.

Longmire, E.K., Eaton, J.K., 1992. Structure of particle laden round jet. J. Fluid Mech 236, 217–257.

Lotfy, A., Rockwell, D., 1993. Near wake and oscillating trailing edge. J. Fluid Mech 251, 173–201.

Maxey, M.R., Riley, J.J., 1983. Equation of motion for a small rigid sphere in a uniform flow. Phys. Fluids 26 (4), 883–889.

Soria, J., Cantwell, B.J., 1994. Topological visualisation of focal structures in free shear flows. Applied Sci. Res 53, 375–386.

Tang, L., Wen, F., Yang, Y., Crowe, C.T., Chung, J.N., Troutt, T.R., 1992. Self-organizing particle dispersion mechanism in a plane wake. Phys. Fluids A 4 (10), 2244–2251.

Troutt, T.R., Scheelke, B., Norman, T.R., 1984. Organized structures in a reattaching separated flow field. J. Fluid Mech 143, 413–427.

Wen, F., Kamalu, N., Chung, J.N., Crowe, C.T., Troutt, T.R., 1992. Particle dispersion by vortex structures in plane mixing layers. ASME J. Fluids Engr 114, 657–666.

Wygnanski, I., Champagne, F., Marasli, B., 1986. On the large-scale structures in two-dimensional small-deficit, turbulent wakes. J. Fluid Mech 168, 31–77.

Yang, Y., Chung, J.N., Troutt, T.R., Crowe, C.T., 1992. The effects of particles on stability of a two-phase wake. Int. J. of Multiphase Flow 19 (1), 137–149.

Yang, Y., 1993. Particle dispersion by coherent vortex structures in a bluff-body wake flow. Ph.D. dissertation, Washington State University.